J Mater Sci (2009) 44:4360–4369
DOI 10.1007/s10853-009-3652-z

Synthesis and characterization of WO_3 and WS_2 hexagonal phase nanostructures and catalytic test in sulfur remotion

**R. Huirache-Acuña · F. Paraguay-Delgado ·
M. A. Albiter · L. Alvarez-Contreras ·
E. M. Rivera-Muñoz · G. Alonso-Núñez**

Received: 18 February 2009 / Accepted: 30 May 2009 / Published online: 16 June 2009

Abstract The aim of the present study was the synthesis and characterization of WO_3 and WS_2 nanostructures in hexagonal phases and the evaluation of the latter as catalyst in the dibenzothiophene hydrodesulfurization reaction. 2H-WS_2 nanostructures were obtained from a precursor WO_3 nanostructure by a two-step hydrothermal/gas phase reaction under well-controlled conditions. All nanostructures were characterized by X-ray powder diffraction, scanning electron microscopy, transmission electron microscopy, and the specific surface area of the materials was measured using the BET method. The catalytic activity and selectivity measurements of the resulting unsupported WS_2 nanocatalysts are also presented. Catalytic activity was found to be highest for the 2H-WS_2 from the WO_3 nanostructure sulfided at 773 K (rate constant of 3×10^{-7} mol/g s).

R. Huirache-Acuña (✉) · E. M. Rivera-Muñoz
Centro de Física Aplicada y Tecnología Avanzada,
Universidad Nacional Autónoma de México,
A.P. 1-1010, Querétaro, Qro C.P. 76000, Mexico
e-mail: rafael_huirache@yahoo.it

F. Paraguay-Delgado · L. Alvarez-Contreras
Centro de Investigación en Materiales Avanzados, S. C.,
CIMAV, Miguel de Cervantes 120, Complejo Industrial
Chihuahua, Chihuahua, Chihuahua 31109, Mexico

F. Paraguay-Delgado
National Institute for Nanotechnology, 11421 Saskatchewan
Drive, Edmonton, AB T6G 2M9, Canada

M. A. Albiter
Facultad de Ingeniería Química, Universidad Michoacana de San
Nicolás de Hidalgo Ciudad Universitaria, Morelia, Michoacán
58060, Mexico

G. Alonso-Núñez
Centro de Nanociencias y Nanotecnología, Universidad
Nacional Autónoma de México, Ensenada, Baja California,
Mexico

Introduction

Transition metal dichalcogenides TX_2 (T = transition metal of group IVB, VB, and VIB, chalcogen, i.e., S, Se, and Te) constitute a structurally and chemically well-defined family of compounds [1]. Their uses range from photoactive materials in photoelectrochemical solar cells, to cathodes in solid state lithium batteries, due to their ability to intercalate with lithium ions [1, 2], to lubricants for tribological applications [3], and catalysts [4].

Studies on hydrodesulfurization (HDS) catalysts are nowadays stimulated by the increase in environmental regulations to reduce the amount of sulfur in vehicle transportation fuels [5, 6]. Thus, HDS catalysts are required to be ever more effective. As is well known, a common approach to increase the number of active sites on catalysts is to decrease their particle size to nanostructured materials. For this reason, increasing research has been focused on nanomaterials to be used as HDS catalysts [7–9]. To date, molybdenum and tungsten sulfides are well-known hydrotreating catalysts, used for decades in the treatment of heavy crude oils to eliminate heteroatoms such as sulfur and break-down aromatic molecules [10].

Various strategies have been used for the synthesis of WS_2 nanostructures. For example, WS_2 tubes have been synthesized from $W_{18}O_{49}$ rods produced by heating tungsten foil at high voltages under argon flow in the presence of SiO_2 [11], by the reaction of hexacarbonyl $W(CO)_6$ as precursor with H_2S in argon in a microwave plasma [12], by burning tungsten wire in low-oxygen-partial pressure atmosphere in argon gas [13], and by template self-assembly of anionic tungstates (WS_4^{-2}) and cationic surfactant molecules such as cetyl trimetyl ammonium (CTA^+) in solution under appropriate conditions [14]. Recently, WO_3 was found to be a versatile precursor in the synthesis of nanostructured WS_2 [15–18]. A conventional method to obtain this kind of material includes the conversion of the respective oxide to sulfide by using a reductive atmosphere such as hydrogen sulfide [4, 19]. In this article, we describe the synthesis and characterization of WS_2 nanostructures by using WO_3 in nanostructured form as precursor and a two-step hydrothermal/gas phase reaction method. Additionally, the catalytic properties of this sulfide nanostructure are discussed.

Experimental

Synthesis of WO_3 and WS_2 nanostructures

Hexagonal WO_3 nanostructures were synthesized by using a hydrothermal route. For this, a saturated aqueous solution of ammonium metatungstate $[(NH_4)_{10}W_{12}O_{41}\ xH_2O]$ (0.15 mol of W) was prepared and acidified with HNO_3 2.2 N (pH around 5). It was then kept in a hermetically sealed flask with stirring for 48 h at 333 K. Subsequently, 5 mL of this aged solution were deposited into a Teflon-lined stainless steel autoclave and heated at 473 K for 48 h. The resulting material was filtered, washed, and dried at room temperature.

To obtain the WS_2 nanostructures, the WO_3 precursor was placed in a tubular reactor and then sulfided for 4 h under a flow of H_2S/H_2 (15% H_2S) at different temperatures: 673, 773, and 1,073 K. Next, the samples were cooled down to room temperature under nitrogen flow. The nanostructures were labeled WS_2-673-K, WS_2-773-K, and WS_2-1073-K, according with the temperature set to obtain the material.

Characterization of samples

A scanning electron microscope (SEM) JEOL JSM 5800 LV was used to study the morphological analysis, images were acquired by secondary electrons and transmission electron microscopy (TEM) Philips trade mark model CM200 operated at 200 kV with a LaB_6 filament was used to study the microstructure and elemental composition distribution using the scanning mode (STEM). Elemental mapping images were obtained with spot size around 2 nm, total time of data acquisition was around 4 min, this time was less than the drift rate of the sample, study samples show high stability to the electron radiation, but we do not study in detail the damage. It is well known that the electron irradiation technique can achieve phase transformation in alloys and compounds through unique non-thermal processes [20–23]. Recently, electron irradiation-induced phase change in tungsten was examined by in situ high resolution electron microscopy [24]. X-ray diffraction (XRD) studies was made with a Philips X Pert MPD diffractometer, equipped with a graphite monochromator, copper Kα radiation with wavelength $\lambda = 1.54056$ Å, operated at 43 kV and 30 mA. Specific surface area (SSA) was determined with a Quantachrome AUTOSORB-1 model by nitrogen adsorption at 77 K using the BET isotherm. Samples were degassed under flowing argon at 473 K for 2 h before nitrogen adsorption.

Catalytic activity and selectivity

In this work, the HDS of dibenzothiophene (DBT) was performed in a 1L volume Parr model 4560 high-pressure batch reactor equipped with magnetically driven turbine, which allows homogeneous dispersion of the gas into the liquid phase. One gram of the WS_2 nanostructures was placed in the reactor with a solution of 5 vol.% of DBT in decaline (total volume 150 mL). The reactor was first purged and then pressurized to 3.1 MPa with hydrogen and heated to 623 K at a rate of 10 K/min, with stirring speed of 600 rpm. After the working temperature was reached, sampling for chromatographic analysis was performed during the course of each run to determine conversion versus time dependence. The reaction was followed for 5 h with sampling of the reaction mixture every 30 min. Reaction products were analyzed using a Perkin-Elmer Clarus 500 gas chromatograph provided with an autosampler and a 9-ft length and 0.125-in. of diameter packed column containing 3% OV-17 as separating phase on Chromosorb WAW 80/100.

Results and discussion

Owing to the structure of ammonium metatungstate to convert ${W_{12}O_{41}}^{10-}$ anions to neutral $W_{12}O_{36}$, excess divalent oxygen anions must be removed during the aging of the precursor solution and hydrothermal treating. Stoichiometrically, five divalent oxygen anions per ${W_{12}O_{41}}^{10-}$ must be combined with protons from the acidic medium:

$$ {W_{12}O_{41}}^{10-} + 10H^+ \rightarrow 12WO_3 + 5H_2O\ . \qquad (1)$$

In reaction 1, high concentrations of both ${W_{12}O_{41}}^{10-}$ and H^+ shift the reaction to the right ensuring the formation of WO_3, although many intermediate steps and thus compounds and phases may exist. The resulting oxide was used as precursor to obtain WS_2 through ex situ activation.

The thermal transformation from WO_3 to WS_2 is represented in Fig. 1, and in Eqs. 2 and 3 as follows:

$$WO_3 + H_2 \rightarrow WO_2 + H_2O, \tag{2}$$

$$WO_2 + 2H_2S \rightarrow WS_2 + 2H_2O. \tag{3}$$

During the sulfidation of tungsten oxide nanoparticles, the first sulfide layer passivates the nanoparticle and prevents coarsening of the nanoparticles into larger platelets. In the next slow step, the partially reduced oxide core is converted into metal-sulfide in a quasi-epitaxial layer by a layer process [25]. It is hypothesized that the hydrogen and oxygen may diffuse through the layers in the radial direction, while sulfur atoms intercalate and diffuse easily along the WS_2 layers until they reach a dislocation, which permits them to diffuse in the radial direction through the layer to the next inner layer [26].

The XRD pattern of the WO_3 nanostructures is presented in Fig. 2a and was indexed based on a hexagonal cell for tungsten trioxide (ICSD 32,001, JCPDS 33-1387; $a = 7.298$ Å, $c = 3.899$ Å, space group P6/mm) [16, 27]. Furthermore, XRD was a suitable technique to obtain information about the sulfidation process. In this work, we observed that in all cases the intensity peaks for the precursor WO_3 (Fig. 2a) disappear after being treated with H_2S/H_2 at temperatures of 673, 773, and 1,073 K, and WS_2 nanostructures were generated.

WS_2 belong to the Group VI family of transition metal dichacolgenides [28]. They form an extremely non-isotropic solid with a layered-type structure. The molecular layer S–W–S shows trigonal symmetry where the transition metal atom is coordinated by six sulfur atoms situated at the corner of a trigonal prism. The molecular layers can be stacked in two ways, as a hexagonal polytype 2H with two molecular layers, and as a rhombohedral polytype 3R. In this case, XRD patterns of WS_2 nanostructures synthesized at different temperatures present a tungstenite-2H structure, as reported in Fig. 2b. In previous studies, the activity of

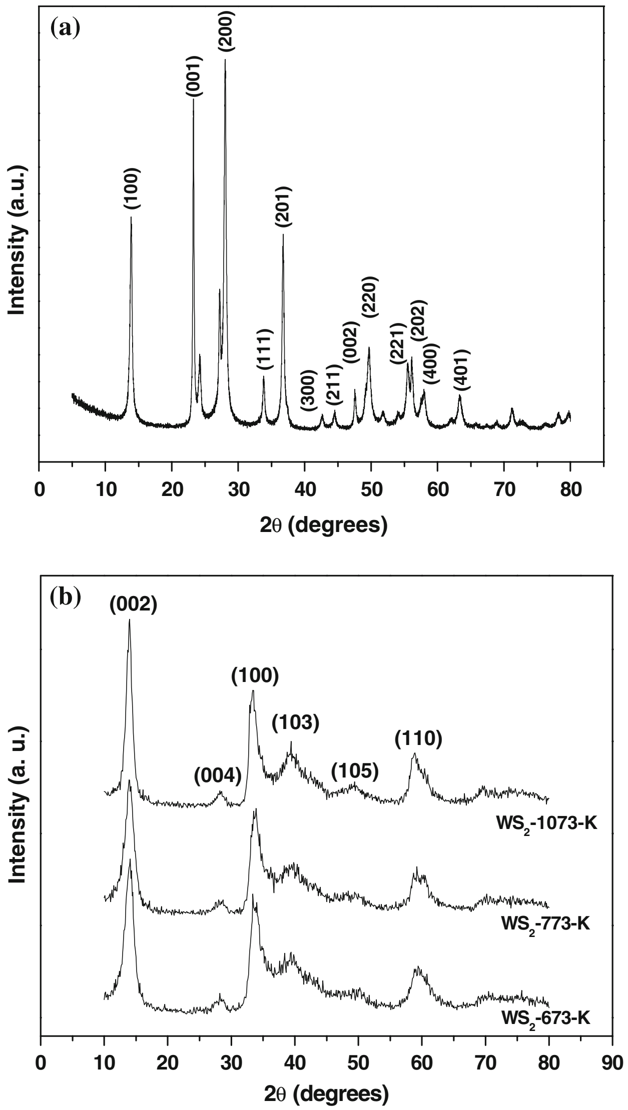

Fig. 2 XRD patterns for: **a** WO_3 nanostructure (indexation based in a hexagonal cell of tungsten trioxide), **b** WS_2 nanostructures synthesized at different temperatures, where (002), (004), (100), (105), (103), and (110) represent the planes from 2H-WS_2 structure

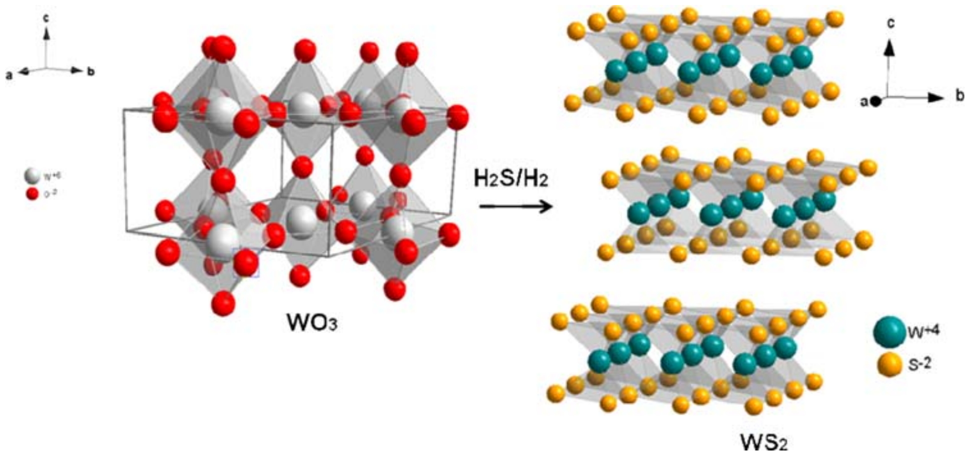

Fig. 1 Transformation scheme for WO_3 into WS_2

tungsten sulfide-based catalysts was shown to strongly depend on the type of crystalline planes (sites) exposed at the surface, owing to the different chemical environments present in each crystallographic orientation [29]. For this reason, it was important to determine the structure of this kind of material. In this study, all diffraction patterns for the 2H-WS_2 phase showed a poor crystalline structure (JCPDS-ICDD 8-237), with a (002) signal at $2\theta \approx 14°$. At this respect, the intensity of the (002) signal is representative of the "*c*" direction layer stacking. The (002) peak for sample WS_2-673-K was higher compared with that presented by the sample WS_2-773-K, and it increased significantly at the highest activation temperature (1,073 K). The different intensities of this peak depend on the experimental conditions used in this work and the activation method. As described by Chianelli [30], the thick and the layers dimension from poor crystalline dichacolgenides can be modified by varying the conditions of preparation. In this study, a higher sulfidation temperature (1,073 K) induced a greater degree of crystallization. Furthermore, a broad envelope beginning approximately at $2\theta = 30°$ and continuing out to above $2\theta = 65°$ was observed. This envelope contains the (100), (103), and (110) reflections. The asymmetric shape of the (100) envelope is characteristic of random layer lattice structures in which layers are displaced randomly with respect to one another. On the other hand, we used a procedure based on the Williamson–Hall equation to calculate microstrain and crystalline size of each sample. The Williamson–Hall equation is:

$$B\mathrm{Cos}\theta = \frac{K\lambda}{t} + 2\varepsilon\mathrm{Sin}\theta, \tag{4}$$

where B is the full width at half maximum (FWHM) of the XRD peaks, K the Scherrer constant, t the crystalline size, λ the wave length of the X-ray, ε the microstrain, and θ the Bragg angle. In this method, $B\mathrm{Cos}\theta$ is plotted against $2\mathrm{Sin}\theta$. Using a linear extrapolation to this plot, the intercept gives the crystalline size and slope gives the microstrain [31]. The effect of synthesis temperature upon crystal size and microstrain are presented in Table 1. At this respect, it was observed that using a synthesis temperature of 773 K, a decrease of average crystallite size is presented (6 nm), compared with their 673 and 1,073 K counterparts (7.3 and 12.8 nm, respectively). Surprisingly, a similar effect was observed for microstrain. Thus, in this work, it seems that temperature of 773 K partially relieve a slightly larger amount of the internal microstrain. XRD diffractograms show a shift of the (002) peak intensity, which could be related with a lattice modification between two adjacent WS_2 slabs along the *c*-axis, as observed in TEM (Fig. 5d), which is attributed to the strain in the bent layers [26]. On the other hand, a correlation between crystal size and catalytic activity might be envisaged. As it is well known, a common approach to increase the number of active sites on catalysts is to decrease the particle and crystal size [32, 33].

Table 1 Crystallite size and microstrain determined by Williamson–Hall method

	Crystallite size (nm)	Microstrain (%)
WS_2-673-K	7.3	2.86
WS_2-773-K	6.0	2.37
WS_2-1073-K	12.8	3.07

WS_2 and MoS_2 layered transition metal dichalcogenides have been found to form spherical and cylindrical crystals of similar geometry to carbon fullerenes and nanotubes [25, 26]. In materials with low-dimensional structures, the instability of weakly bonded crystalline sheets against folding and the saturation of dangling bonds in self-terminated planes stabilize spherical or cylindrical crystal shapes in contrast to flat geometry [34]. In this study, a two-step hydrothermal/gas phase reaction method was used under well-controlled conditions to obtain tungsten sulfide nanostructures. We found that the conditions reported here favor irregular growth of tungsten sulfide nanostructures with a slight evidence of fullerene formation but not throughout the structure. Figure 3a–d shows SEM micrographs of WO_3 and WS_2 nanostructures. Nanostructure morphology is very similar after sulfidation of hexagonal WO_3 to 2H-WS_2 catalysts, as observed in Fig. 3a, c. Figure 3b, d shows higher magnification views of some particles with a high concentration of protruding "spikes" or urchin-like structures formed by self-assembly of numerous nanostructures.

Transmission electron microscopy micrographs of WO_3 and WS_2 nanostructures at different magnifications are reported in Figs. 4a–d and 5a–h, respectively. A representative TEM image of the tungsten oxide nanostructures is shown in Fig. 4a. The sample consists of not very well separated nanoparticles of rectangular and truncated shape and lengths between 30 and 500 nm and wide from 20 to 90 nm, which aggregated because of the high surface energy due to their nanosize. The HRTEM image of the WO_3 nanostructure shows a lattice distance of 0.39 nm, which is very similar to the *d*-spacing of (001) reported for the WO_3 hexagonal cell [27]. This result confirms that the growth of these nanostructures occurs along the *c*-axis direction. Although the SEM micrographs show nanoparticles of WO_3 and WS_2 with very similar morphology, in TEM images the nanostructures presented a different shape. The shape variations within a particular sample of WS_2 nanostructures were greater than shape variations shown by different samples each prepared at a particular sulfidation temperature (Fig. 5a, e). Typical WS_2 fringes (S–W–S layers) were visible on the samples with irregular

Fig. 3 Representative SEM images: **a** micrograph of WO_3 nanostructures, **b** higher magnification of tungsten oxide nanostructures, **c** after sulfidation a very close morphology was observed, **d** higher magnification for sample synthesized at 773 K

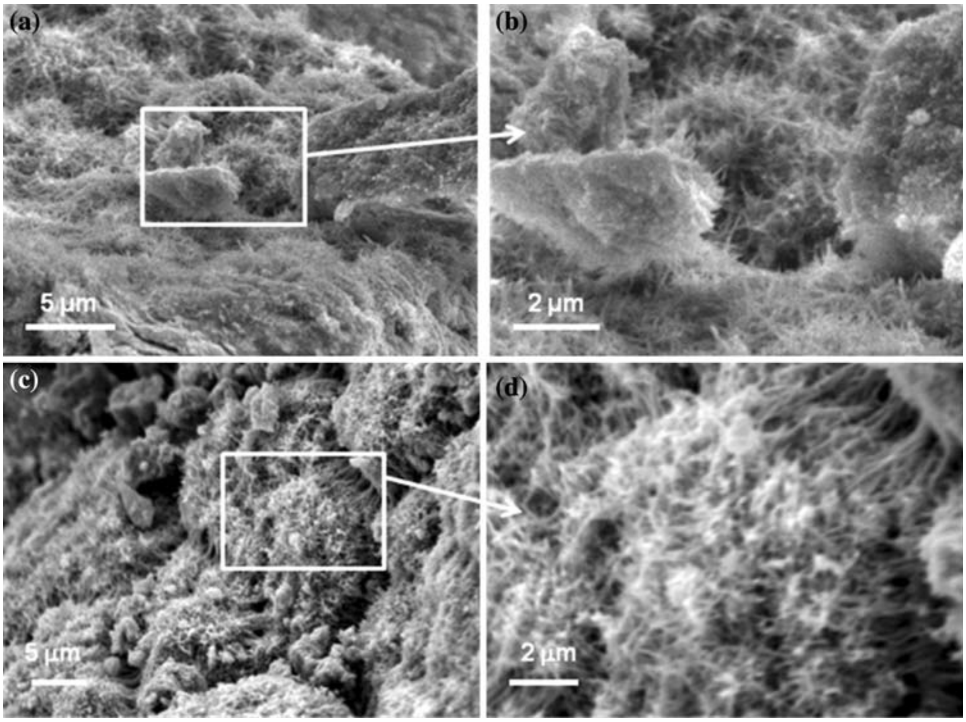

Fig. 4 **a** and **b** TEM image of tungsten oxide nanostructures, **c** and **d** HRTEM image of WO_3 nanostructure showing the growth direction

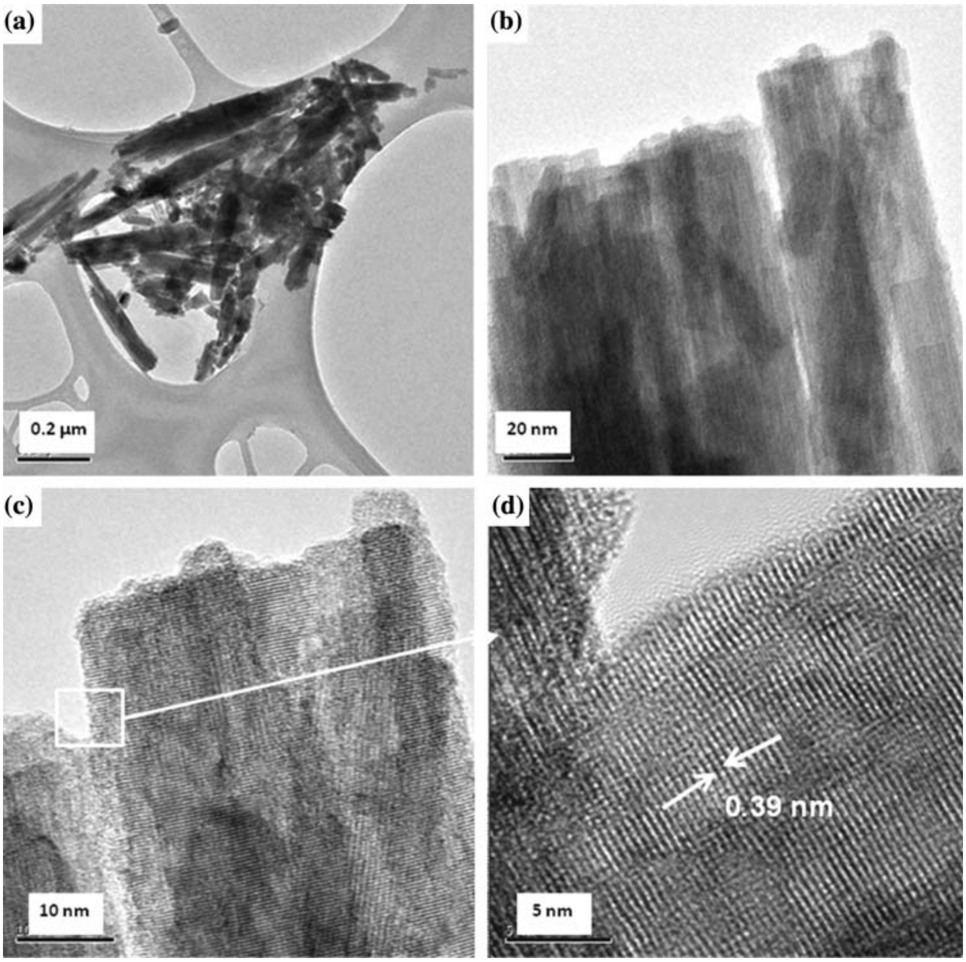

Fig. 5 **a–d** TEM images of WS_2 nanostructures synthesized under a flow of H_2S/H_2 at 773 K and **e–h** at 1,073 K

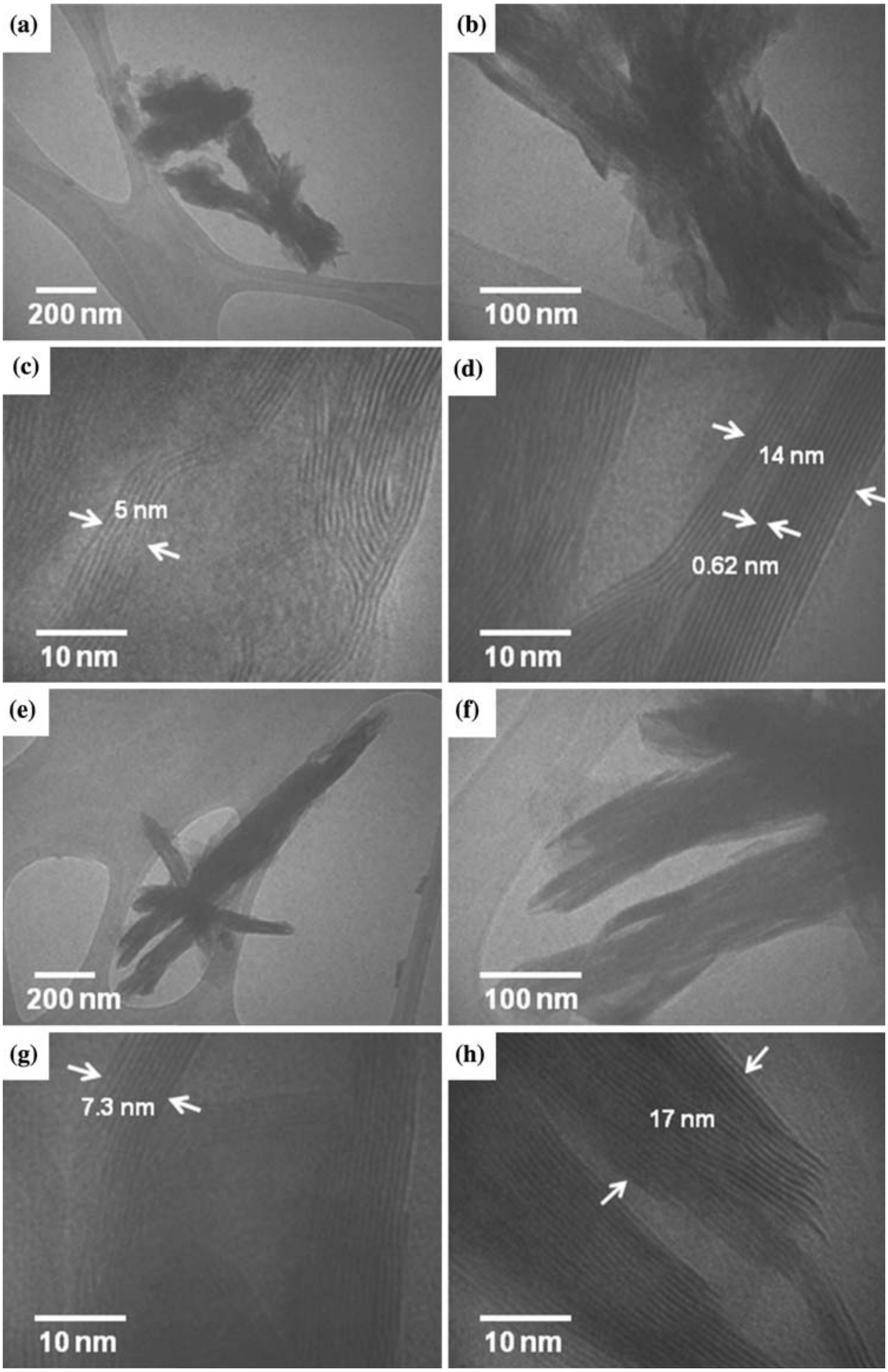

edges. The inter-planar spacing measured for WS_2 along the "*c*" direction was ~0.62 nm, which is close to the reported value for (002) planes (0.618 nm). The slab length of fringes for WS_2-773-K and WS_2-1073-K samples in a particular region is shown in Fig. 5c, d, g, h. Figure 5h illustrates the WS_2 multilayers, one end of which is being cleaved. TEM images show a gradual evolution from a smooth surface (WO_3) to a rough material (WS_2) presenting some hollows as a result of phase change during the sulfidation process.

Figure 6a, b shows scanning transmission microscopy (STEM) elemental mapping images of tungsten (W), oxygen (O), and sulfur (S) before and after sulfidation process, respectively. Images on Fig. 6a show mapping of

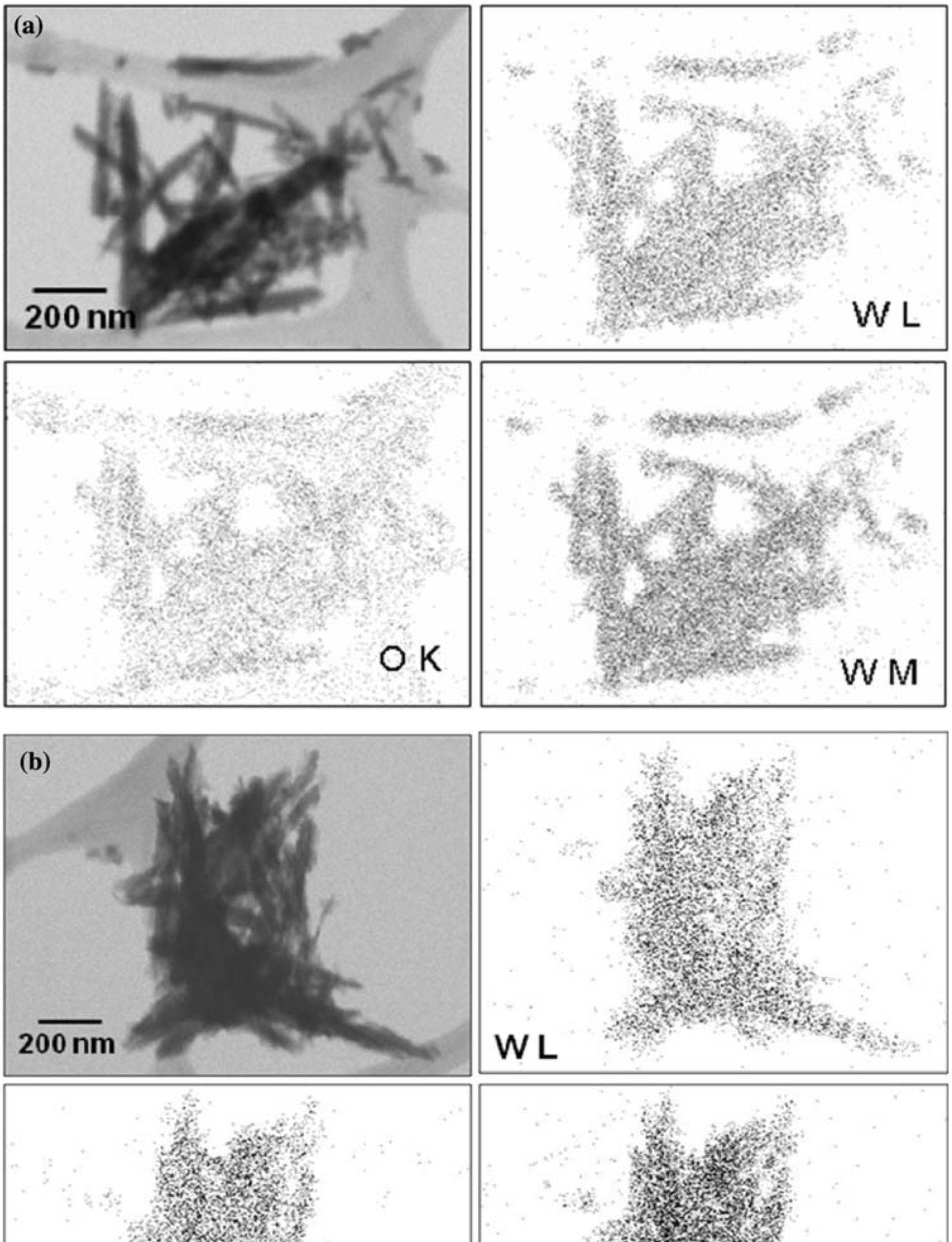

Fig. 6 STEM elemental mapping by EDS for samples: **a** before sulfidation and **b** after sulfidation

the WO_3, it can be noticed the presence of W (L and M transition) and O from the same place of the particles. Figure 6b shows mapping image of the material after sulfidation, these images represent W and S, respectively. This result is clear evidence about the sulfidation process, it means that the oxygen content was substituted by the sulfur element and rearrange its structure as showed by XRD study of the materials.

Pore diameter and SSAs for WS_2 nanostructures are shown in Table 2. The SSA values decreased for all materials after conversion of WO_3 to 2H-WS_2 as a result of phase change. Furthermore, all samples showed a slight decrease in surface area after the HDS catalyst test. This behavior may be related to pore blocking because of carbon deposit formation on the surface, and a particle-sintering effect caused by the temperature and pressure used in the

Table 2 Specific surface area and pore diameter applying the BET method

Sample	Before HDS		After HDS	
	Specific surface area (m^2/g)	Pore diameter (Å)	Specific surface area (m^2/g)	Pore diameter (Å)
WO_3	35.32	18–200	–	–
WS_2-673-K	23.00	18–200	21.03	18–200
WS_2-773-K	29.63	18–200	22.80	18–200
WS_2-1073-K	21.97	30–200	20.68	23–200

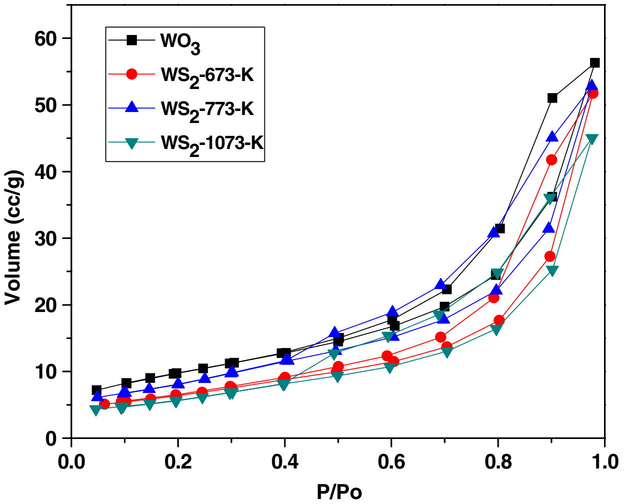

Fig. 7 N_2 adsorption–desorption isotherms at 77 K of the WO_3 and WS_2 nanostructures

HDS reaction. In some cases, the structure of a catalyst subjected to HDS experimental conditions collapses or becomes agglomerated, as mentioned recently [35]. The SSA of the nanostructures studied here was influenced by the different temperatures used in the gas phase decomposition step. WS_2 nanostructures presented an average pore diameter between 18–200 and 20–200 Å. Figure 7 shows the N_2 adsorption–desorption curves corresponding to type IV isotherms with a desorption step characteristic of mesoporous materials above the relative pressure of 0.4 and cylindrical pores open at both sides.

Dibenzothiophene is an appropriate model compound to be used in our experiments due to its difficulty for HDS and because it has been widely used in the literature, which facilitates the comparison with previously reported data. It is known that the reactivity of sulfur compounds follows the order:

thiophene > benzothiophene > dibenzothiophene.

The catalytic activity and selectivity (hydrogenative pathway (HYD)/desulfurization pathway (DDS)) at 5 h of reaction for all catalysts are reported in Table 3. The experimental constant rate (pseudo-zero-order because DBT concentration decreased linearly with time) is given in moles of DBT transformed per second in 1 g of catalyst, and it was calculated from the experimental slope of the plots of DBT concentration versus time, where 34 mmol is the initial concentration of DBT as shown in Eq. 5:

Table 3 Reaction rate constants (*k*) and selectivity (HYD/DDS) at 5 h of reaction

Sample	*k* (mol/g s)	HYD/DDS
WS_2-673-K	2.5×10^{-7}	2.32
WS_2-773-K	3.0×10^{-7}	1.75
WS_2-1073-K	1.6×10^{-7}	1.55

$$[\mathrm{Slope}(1/\mathrm{h})] \times (\mathrm{h}/3600\,\mathrm{s}) \times (1\,\mathrm{mol}/1{,}000\,\mathrm{mmol}) \times (34\,\mathrm{mmol}) \times (1/\mathrm{g}_{\mathrm{catal}}). \quad (5)$$

The HDS of DBT yields biphenyl (BP) through the so-called direct DDS and cyclohexylbenzene (CHB) and tetrahydrodibenzothiophene (THDBT) through the HYD. THDBT is formed only by hydrogenation of one of the aromatic rings of DBT, whereas BP is produced by direct C–S bond cleavage from DBT. Since these two pathways are parallel [36], the selectivity (HYD/DDS) can be approximated calculated by the Eq. 6:

$$(\mathrm{HYD})/(\mathrm{DDS}) = ([\mathrm{CHB}] + [\mathrm{THDBT}])/[\mathrm{BP}]. \quad (6)$$

It has also been shown that the sulfidation conditions affect the final morphology of the product [37], that is the stacking and the edge termination can vary according with the synthesis conditions. The morphology changes expose catalytically active sites, primarily those located at the borders of the nanostructures, thus increasing catalytic activity. A correlation between the SSA and crystal size with the catalytic activity was observed in the present study. A maximum of catalytic activity was observed for the WS_2 nanostructure synthesized at 773 K ($k = 3.0 \times 10^{-7}$ mol/g s, 29.63 m^2/g). This improvement in catalytic activity might be attributed to its slightly larger SSA, which could probably expose a higher amount of active sites. On the other hand, a low crystal size could produce a higher synergized effect [33]. In addition, it is probable that this temperature of reduction (773 K) could largely prevent the closure of the structure. This is very desirable since the closed cage structures would only have basal planes exposed to the reactants in the catalytic activity tests, and they are well known to be inactive in HDS reactions [38]. On the other hand, a lower activity in the HDS of DBT was observed for samples synthesized at 673 K ($k = 2.5 \times 10^{-7}$ mol/g s and 23 m^2/g) and 1,073 K ($k = 1.6 \times 10^{-7}$ mol/g s and 21.9 m^2/g). The activity of the WS_2-773-K sample is very close to that reported by Camacho Bragado et al. [7] (3.7×10^{-7} mol/g s) and by Albiter et al. [8] (3.4×10^{-7} mol/g s) in MoS_2 nanostructured catalysts, tested under similar experimental conditions as used in this report. Furthermore, samples WS_2-673-K and WS_2-773-K are more efficient catalysts than ex situ single layers of MoS_2 [8]. This enhancement in catalytic activity observed for the presently studied samples with respect to the ex situ MoS_2 reference could be related to the morphology and structure change of particles. STM studies have confirmed that special metallic states exist at the edges of small MoS_2 clusters [39] meaning that, when particle size is restricted to a few nanometers (where only edges are present), both the geometric and the electronic configurations will be different and distorted from those in bulk material. It is expected that the nanostructures will undergo a structural rearrangement even though they preserve a resemblance to the macroscopic crystal. STM observations of the interaction between molybdenum sulfide clusters and thiophene indicate activity at the metallic edges, which seems to be terminated by sulfur dimmers [7]. The presence of sulfur dimmers was also discussed by Goodenough [40] as a way to complete the coordination of the molybdenum atoms lying on the surface of molybdenum sulfide. Concerning selectivity, typically low HYD/HDS ratios are commonly observed in industrial CoMo/Al_2O_3 catalysts, favoring the DDS reaction pathway [8]. On the other hand, our values are indeed higher, indicating that hydrogenation reactions occur preferentially. Our results indicate that THDBT continues to be produced and not enough sites may be present for the final C–S bond cleavage to occur; therefore, not all the THDBT can be converted to CHB. The ability of S-saturated edges to donate and accept electrons is believed to enhance catalytic activity, but according with Camacho Bragado et al. [7] they do not seem to be the most favorable sites for the final C–S bond cleavage, since the reaction intermediate (THDBT) was not totally consumed. Since our experimental conditions are close to those used in the industry, we believe that the difference between HYD/DDS ratio is probably due to a difference in the structure of WS_2.

Conclusions

WS_2 nanostructures with hexagonal phase were successfully obtained using a two-step hydrothermal/gas phase method. Nanostructure morphology was modified after sulfidation of hexagonal WO_3 to 2H-WS_2 catalysts and the sulfidation conditions were found to affect the final morphology, structure, and catalytic properties of the WS_2 nanostructures. WS_2-673-K and WS_2-773-K nanostructures were more efficient catalysts than ex situ MoS_2 catalyst (non-nanostructured material) evaluated under similar conditions. All samples show a preference for the hydrogenation (HYD) pathway (selectivity).

Acknowledgments The authors appreciate the valuable technical assistance of C. Ornelas, W. Antúnez, and E. Torres. This work was financially supported by CONACYT 58280-Y, DGAPA-UNAM, IN102509 and postdoctoral scholarship-UNAM. Isabel Pérez Montfort corrected the English version of the manuscript.

References

1. Ouerfelli J, Srivastava SK, Bernède JC, Belgacem S (2009) Vacuum 83:308
2. Tributsch H (1979) Sol Energy Mater 1:257
3. Chinas-Castillo F, Lara-Romero J, Alonso-Nuñez G, Barceinas-Sánchez JDO, Jiménez-Sandoval S (2007) Tribol Lett 26(2):137
4. Alonso G, Chianelli RR (2004) J Catal 221:657
5. Knudsen KG, Cooper BH, Tøpsoe H (1999) Appl Catal A 89:205
6. Park Y, Oh E-S, Rhee H-K (1997) Ind Eng Chem Res 36:5083
7. Camacho Bragado GA, Elechiguerra JL, Olivas A, Fuentes S, Galván D, Yacamán José M (2005) J Catal 234:182–190
8. Albiter MA, Huirache-Acuña R, Paraguay-Delgado F, Rico JL, Alonso-Núñez G (2006) Nanotechnology 17:3473
9. Paraguay-Delgado F, Albiter MA, Huirache-Acuña R, Verde Y, Alonso-Núñez G (2007) J Nanosci Nanotechnol 7(11):3677
10. Olivas A, Alonso G, Fuentes S (2006) Top Catal 37(3–4):175
11. Zhu YQ, Hsu WK, Grobert N, Chang BH, Terrones M, Terrones H, Kroto HW, Walton DRM (2000) Chem Mater 12:1190
12. Vollath D, Szabó V (1998) Mater Lett 35:236–244
13. Kurumada M, Kido O, Sato T, Suzuki H, Kimura Y, Kamitsuji K, Saito Y, Kaito C (2005) J Cryst Growth 275:e1673
14. Li YD, Li XL, He RR, Zhu J, Dheng ZX (2002) J Am Chem Soc 124(7):1411
15. Tenne R, Margulis L, Genut M, Hodes G (1992) Nature 360:444
16. Therese HA, Li J, Kolb U, Tremel W (2005) Solid State Sci 7:67
17. Frey GL, Rothschild A, Sloan J, Rosentsveig R, Popovitz-Biro R, Tenne R (2001) J Solid State Chem 162:300
18. Rothschild A, Popovitz-Biro R, Lourie O, Tenne R (2000) J Phys Chem B 104:8976
19. Liang KS, Chianelli RR, Chien FZ, Moss SC (1986) J Non-Cryst Solids 79:251
20. Strutt ER, Radetic T, Olevsky EA, Meyers MA (2008) J Mater Sci 43:5905. doi:10.1007/s10853-008-2848-y
21. Blanford CF, Carter CB, Stein A (2008) J Mater Sci 43:3539. doi: 10.1007/s10853-008-2550-0
22. Costa PMFJ, Golberg D, Shen G, Metome M, Bando Y (2008) J Mater Sci 43:1460. doi:10.1007/s10853-007-2307-1
23. Cook BA, Wei XZ, Harringa JL, Kramer MJ (2008) J Mater Sci 42:7643. doi:10.1007/10853-007-1898-x
24. Chen CL, Nagase T, Mori H (2009) J Mater Sci 44:1965. doi: 10.1007/10853-009-3302-5
25. Zak A, Feldman Y, Alperovich V, Rosentsveig R, Tenne R (2000) J Am Chem Soc 122:11108
26. Feldman Y, Frey GL, Homyonfer M, Lyakkhovitskaya V, Margulis L, Cohen H, Hodes G, Hutchison JL, Tenne R (1996) J Am Chem Soc 118:5362

27. Ha J-H, Muralidharan P, Kim DK (2009) J Alloys Compd 475(1–2): 446
28. Wilson JA, Yoffe AD (1969) Adv Phys 18:193
29. Kasztelan S (1990) Langmuir 6:590
30. Chianelli RR (1982) Int Rev Phys Chem 2:127
31. Venkateswara Rao K, Sunandana CS (2008) J Mater Sci 43:146. doi:10.1007/s10853-007-2131-7
32. Albiter MA, Huirache-Acuña R, Paraguay-Delgado F, Zaera F, Alonso-Núñez G (2008) J Nanosci Nanotechnol 8(12):6437
33. Huirache-Acuña R, Flores MIZ, Albiter MA, Estrada-Guel I, Ornelas C, Paraguay-Delgado F, Rico JL, Bejar-Gómez L, Alonso-Núñez G, Martínez-Sánchez R (2006) Adv Technol Mater Mater Process 8(2):140
34. Remŝkar M, Mrzel A (2003) Vacuum 71:177
35. Pérez de la Rosa M, Texier S, Berhault G, Camacho A, Yacamán MJ, Mehta A, Fuentes S, Ascencion Montoya J, Murrieta F, Chianelli RR (2004) J Catal 225:288
36. Whitehurst DD, Isoda T, Mochida I (1998) Adv Catal 42:345
37. Lauritsen JV, Bollinger MV, Laegsgaard E, Jacobsen KW, Norskov JK, Clausen BS, Tøpsoe H, Besenbacher F (2004) J Catal 221:510
38. Salmeron M, Somorjai GA, Wold A, Chianelli R, Liang KS (1982) Chem Phys Lett 90:105
39. Bollinger MV, Lauritsen JV, Jacobsen KW, Norskov JK, Helveg S, Besenbacher F (2001) Phys Rev Lett 87:196803
40. Goodenough JB (1982) In: Barry HF, Mitchell P (eds) 4th International conference on the chemistry and uses of molybdenum. Climax Molybdenum, Ann Arbor, MI, p 1